IEEE Access
Multidisciplinary | Rapid Review | Open Access Journal

Received 25 September 2023, accepted 10 October 2023, date of publication 16 October 2023, date of current version 20 October 2023.

Digital Object Identifier 10.1109/ACCESS.2023.3324721

RESEARCH ARTICLE

Toward Inherently Safer Human-Robot Interaction Using Compliant Actuators With High Torque-to-Inertia Ratios and Low Torque-to-Stiffness Ratios

CHEN-PIN YU, CHUN-HUNG HUANG, AND CHAO-CHIEH LAN, (Senior Member, IEEE)
Department of Mechanical Engineering, National Cheng Kung University, Tainan 70101, Taiwan

Corresponding author: Chao-Chieh Lan (cclan@mail.ncku.edu.tw)

This work was supported by the National Science and Technology Council, Taiwan, through NSTC under Project 111-2218-E-006-014.

ABSTRACT Existing robots rely on external sensors to detect and prevent potential human-robot collisions. However, with the growing demand for complex and high-speed human-robot interaction, robots with inherently safer actuators are becoming more desirable. Such robots offer robust protection against excessive impact force even when external sensors fail or become unavailable. Robot actuators with low reflected inertia and low effective stiffness are necessary to achieve mechanically safer human-robot interaction. This paper presents novel compliant actuators with high torque-to-inertia ratios and low torque-to-stiffness ratios without compromising the output torque and output stiffness of an actuator. Comparisons with existing actuators demonstrate that a robot with the proposed compliant actuators has a much lower effective mass sensed at the end-effector. Impact analysis is presented to verify the effectiveness of high torque-to-inertia ratios and low torque-to-stiffness ratios. To assess the performance of the proposed robot, a pose repeatability experiment is conducted, which shows that the end-effector position control precision is comparable to existing stiff robots despite the inherent compliance of the actuators. These compliant actuators can be used to build various human-friendly robots and are expected to improve the safety and reliability of human-robot interaction.

INDEX TERMS Compliant actuator, human–robot interaction, torque-to-inertia ratio, torque-to-stiffness ratio, back-drivability, head injury criterion, repeatability.

I. INTRODUCTION

Robots may consist of either serially or parallel connected actuators [1], [2] to mimic the motion of human arms to perform dexterous manufacturing or daily tasks. With stiff actuators, robots can achieve highly accurate and precise motion that surpasses human workers. Hence, robots are used in factory manufacturing lines to replace human workers performing repetitive or dangerous jobs. The growing emphasis on cost reduction has expanded the role of robots into tasks requiring close interaction with humans in a dynamic or unstructured workspace. To ensure safe human-robot interaction, external optical [3], [4] or force-torque [5], [6] sensors can detect potential human-robot collisions. However, sensor detection and feedback control lead to extra cost and complexity, and are only limited to robots in low-speed operation. Moreover, many external sensors are only valid at specific locations on the robot. Therefore, for robustness consideration, it is crucial for the entire robot body to have inherently safe interaction with a human even when the external sensors fail or become unavailable.

When collisions occur, the excessive impact force between a human and a robot is due to the high linear or angular momentum. Hence, the easiest way to provide inherently safe interaction is to reduce the robot's operation speed. However,

The associate editor coordinating the review of this manuscript and approving it for publication was Wai-Keung Fung.

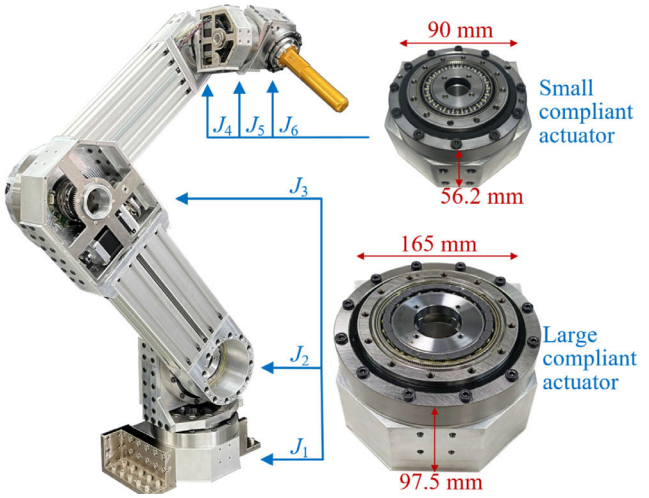

FIGURE 1. Prototype of a robot with the proposed compliant actuators.

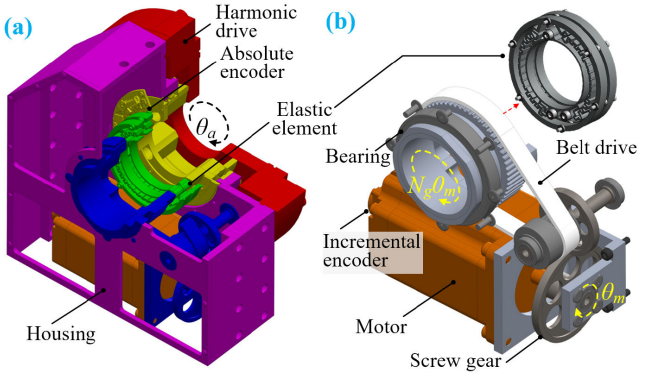

FIGURE 2. (a) The large compliant actuator (b) First geartrain of the large compliant actuator.

a low-speed robot would decrease the interaction efficiency, as human motion is usually faster. Therefore, reducing the effective mass at the point of contact is a more feasible solution. The effective mass of a robot depends on the links and actuators that are serially connected. Because links can always be fabricated using structures with high strength-to-weight ratios [7], the actuator's reflected inertia accounts for most of the effective mass of a robot.

The reflected inertia of an actuator mainly depends on the motor inertia and the transmission ratio. Motors with large-diameter hollow rotors have higher inertia than those with small-diameter solid rotors. Geartrains [8], belt drives [9], and cable drives [10] with low transmission ratios have been developed to reduce the reflected inertia of an actuator. The frictional loss of the actuator can also be reduced, allowing the actuator to be back-drivable. However, a low transmission ratio results in a low actuator output torque. Therefore, it remains challenging to design an actuator with a high transmission ratio and low reflected inertia simultaneously.

To develop a mechanically safer robot actuator without lowering the transmission ratio, an elastic element can be inserted between the actuator and the output link to form a series elastic actuator (SEA) [11], [12], [13], [14], [15], [16], [17], [18], [19]. The elastic element can provide an energy buffer to filter the impact force between humans and robots. Hence, the reflected inertia of the actuator, regardless of the transmission ratio, is decoupled from the output. The elastic element on the actuator output side is usually bulky compared to other actuator components. The performance of SEAs highly depends on the stiffness of the elastic element [20]. An elastic element with a lower stiffness can be more back-drivable and safer. However, a lower stiffness reduces the output position control bandwidth and affects the robot's repeatability. To solve both the problems of control bandwidth and safety, variable-stiffness actuators have been developed [21], [22], [23], [24]. However, additional actuators are required to adjust the output stiffness, which makes variable-stiffness actuators much more complicated than SEAs.

This paper aims to develop a robot using a new type of compliant actuator to achieve inherently safer human-robot interaction. A special type of geartrain is proposed to allow the actuator to have a large-diameter hollow shaft while using a motor with a small-diameter solid rotor. This allows the actuator to have a high torque-to-inertia ratio while signal and power cables can pass through the hollow shaft of the actuator. To overcome the challenges of existing SEAs, the elastic element of the proposed compliant actuator is placed in the middle of the geartrain rather than on the output side of the geartrain. Thus, the output stiffness can remain high while the size of the actuator can remain small. Meanwhile, the reflected inertia of the motor can still be decoupled. In the subsequent sections, the prototype and modeling of the compliant actuators and robot are shown in Sec. II. Sec. II further investigates the torque-to-inertia ratios of the proposed compliant actuators. Sec. III presents the comparison of torque-to-stiffness ratios of various compliant actuators, along with the design and analysis of the elastic elements. In Sec. IV, the effects of reflected inertia and effective stiffness on the impact force are analyzed and experimentally verified. Sec. V further verifies the control performance of the robot and compliant actuators through experiments of pose repeatability. Finally, conclusions are made in Sec. VI.

II. PROTOTYPE AND MODELING OF THE COMPLIANT ACTUATORS AND ROBOT

A. PROTOTYPE OF THE COMPLIANT ACTUATORS AND ROBOT

Fig. 1 illustrates a serial robot built using six proposed compliant actuators. The robot configuration is like existing collaborative robots, such as the Universal Robot [25]. Three large compliant actuators are used for the first three joints ($J_1 \sim J_3$). Another three small compliant actuators are used for the last three joints ($J_4 \sim J_6$). The compliant actuators are joined using aluminum extrusions to reduce weight without compromising rigidity. Each compliant actuator is equipped with a hollow shaft to facilitate convenient cable routing. The robot in Fig. 1 has a mass of 29 kg.

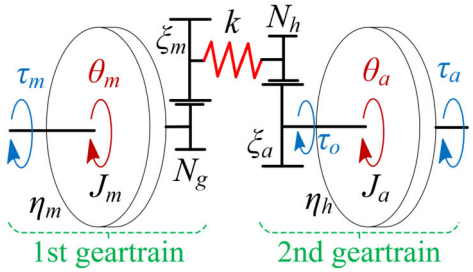

FIGURE 3. Dynamic model of the compliant actuator.

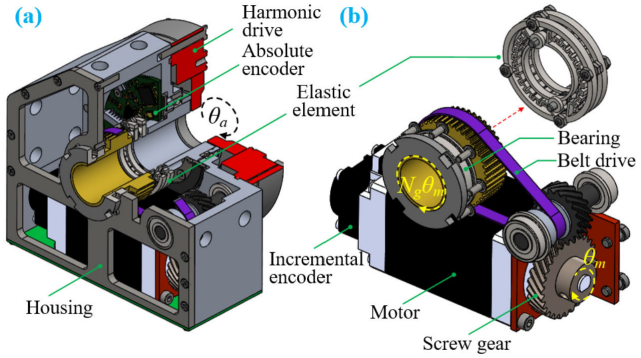

FIGURE 4. (a) The small compliant actuator (b) First geartrain of the small compliant actuator.

TABLE 1. Specifications of the large and small compliant actuators.

Specification	Large (J_1~J_3)	Small (J_4~J_6)
Total mass (kg)	5.8	0.9
Size (mm^3)	165×176×97	90×85×56
Inner hole diameter (mm)	40	15
Gear ratio N_g×N_h	2×51	2×101
1st geartrain reflected inertia (kgm^2)	1.03	0.194
2nd geartrain reflected inertia (kgm^2)	1	0.11
Total reflected inertia (kgm^2)	2.03	0.304
Maximum continuous torque (Nm)	255	38.4
Moment rigidity (Nm/rad)	145×10^4	12.7×10^4
Elastic element stiffness k (Nm/rad)	14.97	1.13
Flex spline stiffness k_f (Nm/rad)	8.8×10^4	8400
Maximum speed (°/s)	102	125

TABLE 2. Distribution of the reflected inertia of the compliant actuators (Unit: kgm^2).

Category	Component	Large (J_1~J_3)	Small (J_4~J_6)
First geartrain	Motor's rotor	0.520 (25.6%)	0.073 (24.0%)
	Screw gears	0.187 (9.2%)	0.065 (21.4%)
	Elastic element	0.097 (4.8%)	0.010 (3.3%)
	Others	0.226 (11.1%)	0.050 (16.4%)
Second geartrain	Wave generator	0.741 (36.5%)	0.055 (18.1%)
	Encoder ring set	0.162 (8%)	0.037 (12.2%)
	Others	0.097 (4.8%)	0.014 (4.6%)
Total		2.03 (100%)	0.304 (100%)

B. MODELING OF THE LARGE AND SMALL COMPLIANT ACTUATORS

As shown in Fig. 2(a), the large compliant actuator includes a motor (PKP268D42A2, Oriental Motor) and two geartrains. Fig. 2(b) shows the first geartrain. A screw gear pair and a belt drive collectively provide a gear ratio of N_g. This arrangement makes the motor rotation θ_m and the input of the second geartrain perpendicular to one another. The second geartrain employs a harmonic drive (SHD-40, Harmonic Drive) with a gear ratio of N_h from the wave generator to the circular spline. The output rotation is denoted by θ_a. An elastic element connects the two geartrains, as illustrated in Fig. 2(b). The elastic element is used to filter the motor inertia from the actuator output. Fig. 3 shows the equivalent dynamic model of the large compliant actuator. The equations governing the first and second geartrains can be respectively formulated as follows [26].

$$J_a\ddot{\theta}_a + \xi_a\dot{\theta}_a + \eta_h N_h k(N_h\theta_a - \theta_m/N_g) = \tau_a \quad (1)$$

$$J_m\ddot{\theta}_m + \xi_m\dot{\theta}_m/N_g^2 + k(\theta_m/N_g - N_h\theta_a)/N_g = \tau_m\eta_m \quad (2)$$

In Eqs. (1)-(2), τ_m and τ_a are the motor and externally applied torques, respectively; J_m and J_a are the equivalent inertias of the first and second geartrains, respectively. Variables η_m and η_h are used to account for the efficiencies of the first and second geartrains, respectively, whereas ξ_m and ξ_a are used to account for the viscous friction of the two geartrains. The stiffness of the elastic element is denoted by k. For clarity of analysis, the stiffness k_f of the flex spline is considered as an environmental stiffness and hence not included in the dynamic equations in Eqs. (1)-(2).

In Eqs. (1)-(2), the motor rotation θ_m is determined through a 15-bit incremental optical encoder. The rotation of the wave generator θ_w is obtained using a 19-bit absolute magnetic encoder. Disregarding rotation stemming from the flex spline's deformation, the output rotation θ_a is equal to $N_h\theta_w$. The encoder values are used to obtain the elastic element's deformation, allowing for its estimation and control of the output torque τ_o, as depicted in Fig. 3.

$$\eta_h N_h k(\theta_m/N_g - N_h\theta_a) = \tau_o \quad (3)$$

where $\theta_m/N_g - N_h\theta_a$ is the deformation of the elastic element. In the static case, we have $\tau_o = -\tau_a$.

The small compliant actuator in Fig. 4(a) has the same configuration and dynamic model as the large compliant actuator, except that the harmonic drive (SHD-17) has a transmission ratio of $N_h = 101$. In Fig. 4(b), the motor used for the small compliant actuator is PKP225D15A2 from Oriental Motor. For both compliant actuators, the inclusion of the elastic element ensures a linear relationship between torque and deformation, thereby offering a high level of torque control resolution.

The specifications of both compliant actuators are listed in Table 1. The motors used for both compliant actuators are hybrid two-phase stepper motors with bipolar drives. It has been reported in [27] that hybrid two-phase stepper motors have much higher torque-to-inertia ratios when compared with other brushed or brushless direct-current motors. In addition, through proper encoder position control [27],

TABLE 3. Comparison of torque-to-inertia ratios.

Actuator type	Max. torque (Nm)	Transmission ratio	Reflected inertia (kgm^2)	Torque-to-inertia ratio (Nm/kgm^2)
Our robot (J_1~J_3)	255	102	2.03	120.56
Our robot (J_4~J_6)	38.4	202	0.304	126.32
UR10 (J_1~J_2)	330	101	10.05	32.84
UR10 (J_3)	150	101	3.01	49.83
UR10 (J_4~J_6)	56	101	0.809	69.22
KUKA LWR4+ (J_1)	200	101	3.19	62.70
KUKA LWR4+ (J_6)	30	101	0.391	76.73

hybrid two-phase stepper motors can achieve accurate and smooth motion control.

In contrast to our earlier work [13], [19], [20], [26] that focused on the force/torque control or impedance control of compliant actuators, this paper focuses on the intrinsic compliance and inertia distribution of compliant actuators and their effects on the human-robot interaction safety and repeatability.

C. INERTIA DISTRIBUTION OF THE COMPLIANT ACTUATORS

Table 2 lists the reflected inertia distribution of both compliant actuators. The components in each actuator are categorized into the first and second geartrains. The reflected inertia and contribution percentage of each component are both calculated at the actuator output. For an actuator to have a large-diameter hollow shaft, the motor's rotor needs to be hollow. Hence, the motor's rotor often accounts for most of the reflected inertia. By contrast, the proposed compliant actuator involves the use of the first geartrain to change the direction of transmission, leading to a large-diameter hollow shaft while using a motor with a small-diameter solid rotor. Hence, the motor inertia can be smaller when compared with motors with hollow rotors (e.g., [6]).

The first geartrain accounts for 65.1% of the total reflected inertia for the small compliant actuator. The reflected inertia of the first geartrain is primarily due to the inertia of the motor's rotor (24.0% of the total reflected inertia). By contrast, the reflected inertia of the second geartrain is primarily due to the inertia of the wave generator (18.1% of the total reflected inertia). The first geartrain accounts for 50.7% of the total reflected inertia for the large compliant actuator. The motor's rotor and wave generator are the two major components that contribute to the total reflected inertia of the large compliant actuator. The first geartrains of both actuators account for more than half of the total reflected inertia. The reflected inertia of the elastic element of each actuator is small and less than 5% of the total reflected inertia. They are accounted for in the reflected inertia of the first geartrain.

D. COMPARISON OF TORQUE-TO-INERTIA RATIOS

Although the torque-to-weight ratio has been used to evaluate the performance of an actuator [28], it is not suitable for assessing the safety performance of actuators with high

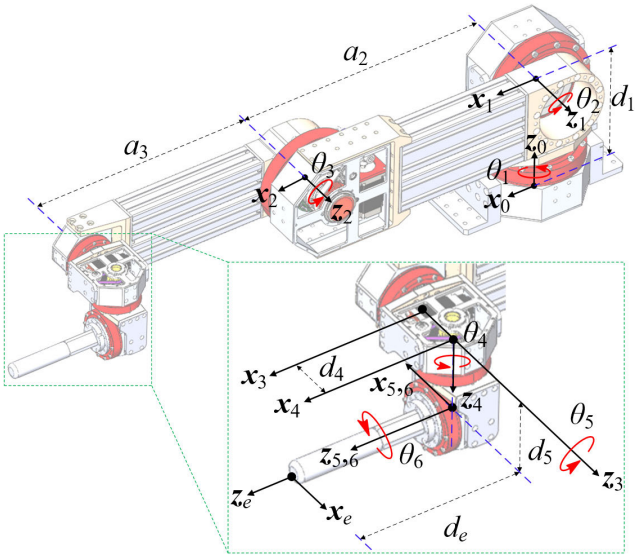

FIGURE 5. Definition of D-H parameters of the proposed robot.

TABLE 4. D-H parameters of the proposed robot.

Frame	θ_i	d_i	a_i	α_i
1	θ_1	d_1 (220.4 mm)	0	−90°
2	θ_2	0	a_2 (612.7 mm)	0°
3	θ_3	0	a_3 (571.6 mm)	0°
4	θ_4	d_4 (65.25 mm)	0	−90°
5	θ_5	d_5 (90 mm)	0	90°
6	θ_6	0	0	0°
e	π	d_e	0	0

transmission ratios. Instead, we define the torque-to-inertia ratio to describe the relationship between the actuator's maximum continuous torque and the reflected inertia on the output side. For a robot to have safer interaction without compromising the output torque, the torque-to-inertia ratios of its actuators should be as high as possible. A high torque-to-inertia ratio also means a high achievable acceleration of the actuator. Table 3 compares the torque-to-inertia ratios of the compliant actuators used in the proposed robot with those of existing collaborative robots. The UR10 robot [29] and KUKA LWR4+ robot [30] were chosen because their actuators have similar output torques and transmission ratios as the compliant actuators of our robot. For our robot, the maximum torque of each actuator is estimated based on the maximum motor torque, transmission ratios, and friction loss of the geartrain.

For the UR10 robot, the maximum torque values are obtained from [31], whereas the values of the reflected inertia are obtained from [29]. Only the inertia values of the motor and wave generator are considered for the UR10 robot. The inertia values of other components are not available in the literature and are not considered. Hence, the actual reflected inertia of the UR10 robot may be higher. The KUKA LWR4+ robot has seven serially connected actuators for the seven joints ($J_1 \sim J_7$). The maximum torque values of the actuators are obtained from [30], whereas the values of the reflected inertia are obtained from [32].

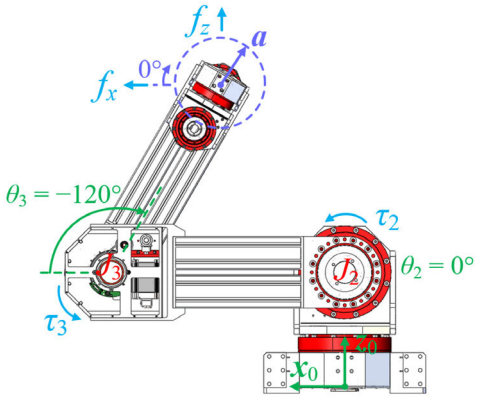

FIGURE 6. Illustration of end-effector acceleration ($\theta_2 = 0°$, $\theta_3 = -120°$).

For the actuators of the first two joints J_1 and J_2, the torque-to-inertia ratio of our robot is nearly four times that of the UR10 robot. For the actuators of the last three joints $J_4 \sim J_6$, the torque-to-inertia ratio of our robot is about two times that of the UR10 robot. In Table 3, the average torque-to-inertia ratio of our robot is also nearly two times that of the KUKA LWR4+ robot. Compared with other actuators in Table 3, the proposed small compliant actuator has a high torque-to-inertia ratio despite a high transmission ratio of 202.

E. EFFECT OF TORQUE-TO-INERTIA RATIO ON THE TORQUE ELLIPSES, FORCE ELLIPSES, AND EFFECTIVE MASS

To illustrate the effect of torque-to-inertia ratios, we compare the torque and force ellipsoids of our robot with those of the UR10 robot. The UR10 robot was chosen because its actuators have comparable torques to those of our robot. The frames of the proposed robot are defined in Fig. 5. The values of $\theta_1 \sim \theta_6$ are all zero in Fig. 5. Table 4 lists the Denavit-Hartenberg (D-H) parameters of the proposed robot. The values of a_2 and a_3 in Table 4 are specifically made equal to those of the UR10 robot, so both robots have the same workspace.

For the forward actuation, we consider a case where the robot actuators generate torques so that the robot end-effector has a linear acceleration with a unit magnitude $\boldsymbol{a}^{\mathrm{T}}\boldsymbol{a} = 1$ m/s^2. Fig. 6 illustrates a unit circle of acceleration in the $\boldsymbol{x}_0\boldsymbol{z}_0$ plane. The equation for the torque ellipsoid can be derived as follows.

$$\boldsymbol{\tau}^T(\boldsymbol{J}_v^T\boldsymbol{\Lambda}\boldsymbol{\Lambda}^T\boldsymbol{J}_v)^{-1}\boldsymbol{\tau} = 1 \tag{4}$$

where τ is the vector containing the actuator torques, $\boldsymbol{J}_v$ is the linear velocity portion of the original Jacobian matrix $\boldsymbol{J}$. Matrix Λ is the translational Cartesian inertia matrix of the robot, which can be related to the mass matrix $\boldsymbol{M}$ as follows.

$$\boldsymbol{\Lambda}(\boldsymbol{\theta}) = \boldsymbol{J}_v^{-T}(\boldsymbol{\theta})\boldsymbol{M}(\boldsymbol{\theta})\boldsymbol{J}_v^{-1}(\boldsymbol{\theta}) \tag{5}$$

where θ is the vector containing the actuator rotation angles. The size and orientation of a torque ellipsoid can be used to characterize the required actuator torques to generate a unit acceleration at the end-effector. The larger the distance from the center to the edge of the ellipsoid, the larger the required actuator torques are.

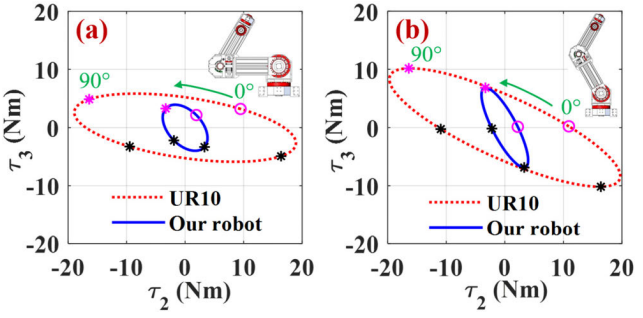

FIGURE 7. Comparison of torque ellipses (a) $\theta_2 = 0°$, $\theta_3 = -120°$ (b) $\theta_2 = -60°$, $\theta_3 = -60°$.

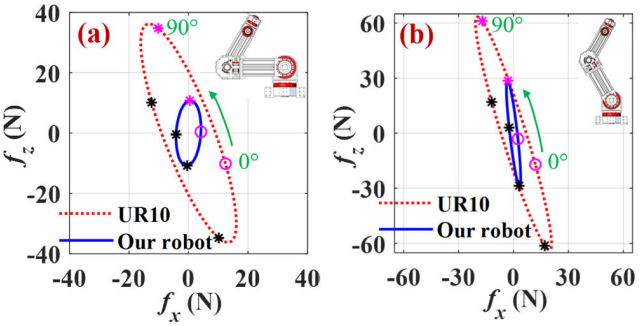

FIGURE 8. Comparison of force ellipses (a) $\theta_2 = 0°$, $\theta_3 = -120°$ (b) $\theta_2 = -60°$, $\theta_3 = -60°$.

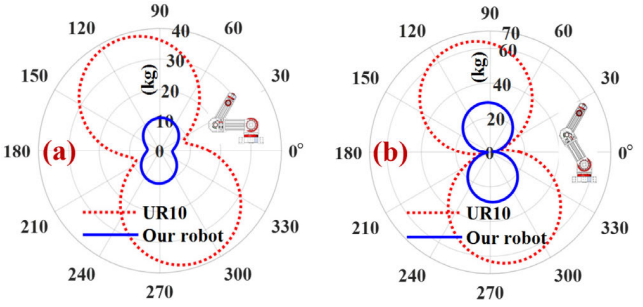

FIGURE 9. Comparison of effective masses (a) $\theta_2 = 0°$, $\theta_3 = -120°$ (b) $\theta_2 = -60°$, $\theta_3 = -60°$.

For the backward actuation, we consider the case where an external force $\boldsymbol{f}$ is applied to the robot end-effector to exhibit a linear acceleration with a unit magnitude $\boldsymbol{a}^{\mathrm{T}}\boldsymbol{a} = 1$ m/s^2. The equation for the force ellipsoid can be expressed as follows.

$$\boldsymbol{f}^T(\boldsymbol{\Lambda}\boldsymbol{\Lambda}^T)^{-1}\boldsymbol{f} = 1 \tag{6}$$

The size and orientation of a force ellipsoid can be used to characterize the required external force to generate a unit acceleration at the end-effector. For a unit acceleration, the size of the force ellipsoid also represents the effective mass of the robot sensed by a human operator at the end-effector. The larger the distance from the center to the edge of the ellipsoid, the larger the effective mass is. Therefore, both the torque and force ellipsoids should be as small as possible to achieve a human-friendly robot.

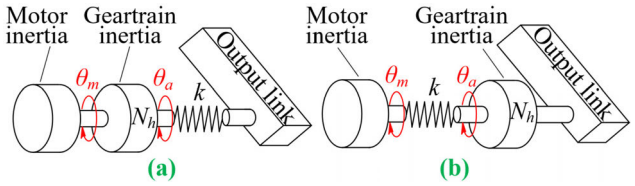

FIGURE 10. (a) Model of existing SEAs (b) Model of the proposed compliant actuator.

For both the proposed robot and the UR10 robot, the actuators of the first three joints have much larger reflected inertia than the actuators of the last three joints. Hence, their effect should be first considered. As an example, only the actuators of J_2 and J_3 are active. Other actuators are fixed. The masses of the links and other actuators are ignored. The deformation of the elastic elements of the actuators is also ignored. Since the end-effector only moves in the z_0z_0 plane, the torque and force ellipsoids reduce to torque and force ellipses. The values of a_2 and a_3 in Table 4 are used to obtain the Jacobian matrix for both our robot and the UR10 robot.

Two different robot postures are considered for analyzing the ellipses. Fig. 6 shows the posture of $\theta_2 = 0°$ and $\theta_3 = -120°$. The other posture is $\theta_2 = -60°$ and $\theta_3 = -60°$. Fig. 7 shows the torque ellipses of both postures. The corresponding torques from J_2 and $J_3$are denoted by τ_2 and τ_3, respectively. The four markers on the edge of an ellipse correspond to the directions of the end-effector acceleration: 0°, 90°, 180°, and 270°. For both subfigures in Fig. 7, the torque ellipses of our robot are much smaller than those of the UR10 robot. Hence, our proposed robot requires much smaller actuator torques for the same end-effector acceleration. For the force ellipses in Fig. 8, the external forces in the x_0 and z_0 directions are denoted by f_x and f_z, respectively. The force ellipses of the UR10 robot are much larger than those of our robot. A larger force ellipse would result in a larger impact force when a collision occurs between a human and a robot.

Based on the force ellipses in Fig. 8, the effective masses of both robots can be obtained in Fig. 9, where the radial coordinate denotes the effective mass and the angular coordinate denotes the direction of end-effector acceleration. For the posture of $\theta_2 = 0°$ and $\theta_3 = -120°$, the maximum effective mass is 10.8 kg for our robot and 38.7 kg for the UR10 robot. For the posture of $\theta_2 = -60°$ and $\theta_3 = -60°$, the maximum effective mass is 28.9 kg for our robot and 65.0 kg for the UR10 robot. Our robot has a significantly lower effective mass at both postures. The effective mass sensed at the end-effector of a robot should be made as small as possible in all directions to be suitable for human-robot interaction.

III. ANALYSIS AND DESIGN OF THE ELASTIC ELEMENT

A. COMPARISON WITH EXISTING SERIES ELASTIC ACTUATORS

In addition to the high torque-to-inertia ratios of the proposed actuators, the elastic element placed between the first and second geartrains also contributes to the safe interaction of the actuators. Fig. 10 shows the models of existing SEAs [11], [12], [13], [14], [15], [16], [17], [18], [19] and our proposed compliant actuators. In Fig. 10(a), an existing SEA uses the elastic element to connect the actuator and the output link. Hence, the effect of motor inertia and geartrain inertia on the output impact force can both be filtered. However, the stiffness of the elastic element needs to be large enough to match the output torque amplified by the geartrain. To provide sufficient impact filtering, the stiffness of the elastic element is usually made much smaller. Hence, existing SEAs are usually too soft and cannot provide good control and repeatability performance. Although the elastic element has a low stiffness, installing the elastic element on the output side of the actuator still requires a significantly large space.

By contrast, Fig. 10(b) shows that the elastic element of the proposed compliant actuator is placed between the motor and the geartrain with a transmission ratio of N_h. The effective stiffness on the actuator output side is equal to $k(N_h)^2$. Since N_h is usually a large number, the stiffness of the elastic element can be made much smaller without significantly reducing the effective stiffness. The elastic element with low stiffness allows the impact filtering of the motor inertia while the actuator output stiffness is not compromised.

TABLE 5. Comparison of torque-to-stiffness ratios.

Actuator type	Maximum torque (Nm)	Effective stiffness (Nm/rad)	Torque-to-stiffness ratio (°)
Our actuator (Large)	255	38937	0.375
Our actuator (Small)	38.4	11527	0.191
Actuator in [14]	50	573	5.0
Actuator in [15]	56	500	6.42
Actuator in [16]	150	4507	1.91
Actuator in [17]	350	4011	5.0
Our first geartrain (Large)	5	14.97	19.14
Our first geartrain (Small)	0.384	1.13	19.47

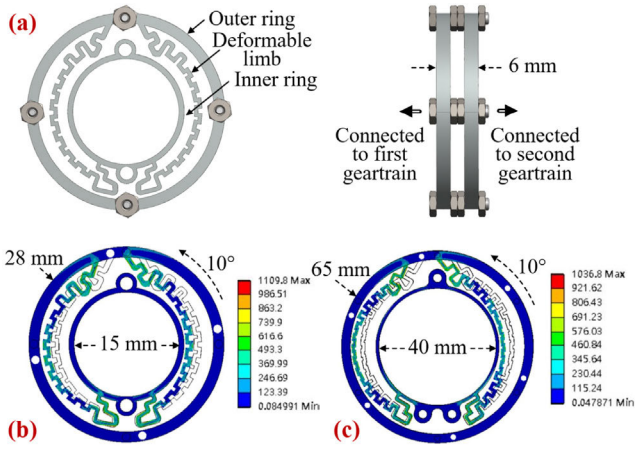

FIGURE 11. (a) Front and side views of the elastic element for the small compliant actuator (b) Shape and deformation of the planar spring for the small compliant actuator (c) Shape and deformation of the planar spring for the large compliant actuator.

TABLE 6. Specifications of the elastic elements.

Specification	Large (J_1~J_3)	Small (J_4~J_6)
Outer diameter (mm)	65	28
Inner diameter (mm)	40	15
Planar spring thickness (mm)	6	2
Elastic element thickness (mm)	14	6
Total stiffness (Nm/rad)	14.97	1.13
Experimental stiffness (Nm/rad)	13.83	1.17
Maximum rotation (°)	±20	±20
Maximum equivalent stress (MPa)	1036.8	1109.8

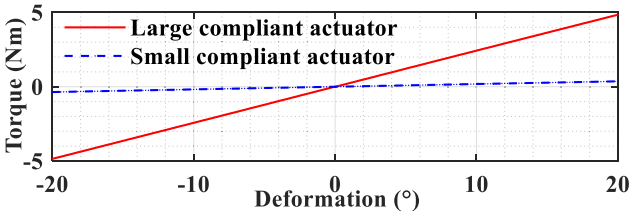

FIGURE 12. Experimental torque-to-deformation curves of the elastic elements.

B. COMPARISON OF TORQUE-TO-STIFFNESS RATIOS

To compare the output stiffness and impact filtering ability of different SEAs, we define the torque-to-stiffness ratio to describe the relationship between the actuator's maximum torque and the effective stiffness on the output side. This ratio also represents the maximum deformation (in degrees or radians) of an SEA when its maximum torque is applied. Table 5 compares the torque-to-stiffness ratios of our compliant actuators with existing SEAs. A lower torque-to-stiffness ratio indicates that the actuator output is stiffer and performs better position control. By contrast, a higher torque-to-stiffness ratio indicates that the actuator is softer and can filter more impact force. In Table 5, the torque-to-stiffness ratios of our large and small compliant actuators are roughly less than 10% of those of existing SEAs [14], [15], [16], [17]. This indicates that our compliant actuators are much stiffer. Hence, the position control response would be faster and more accurate than existing SEAs. Due to high torque-to-stiffness ratios, existing SEAs have better filtering abilities than our compliant actuators. Nevertheless, the motor inertia of our compliant actuator in Fig. 10(b) can still be successfully filtered. The last two rows in Table 5 list the torque-to-stiffness ratios on the output side of the first geartrains of our actuators. Since the ratios are high, the motor inertia can be successfully filtered. According to the inertia distribution in Table 2, the proposed compliant actuators can filter more than half of the actuator inertia while maintaining a high stiffness at the actuator output.

C. DESIGN AND ANALYSIS OF THE ELASTIC ELEMENTS FOR THE PROPOSED COMPLIANT ACTUATORS

Helical springs [14], hollow shafts [15], and planar springs [16], [17] have been used as elastic elements for SEAs. However, the size of the elastic element needs to be relatively large when it is placed on the output side of an existing SEA. Since the proposed compliant actuator only requires the elastic element to have a low stiffness, the size of the elastic element can be relatively small. Fig. 11(a) shows the front and side views of the elastic element for the small compliant actuator. The elastic element includes two identical planar springs that are serially connected on the outer ring to generate a lower stiffness. The two inner rings are respectively connected to the first and second geartrains. The planar springs for the large compliant actuator are connected similarly. Figs. 11(b) and 11(c) show the dimensions of the planar springs used for the small and large compliant actuators, respectively. The central hole of each planar spring is used for cable routing.

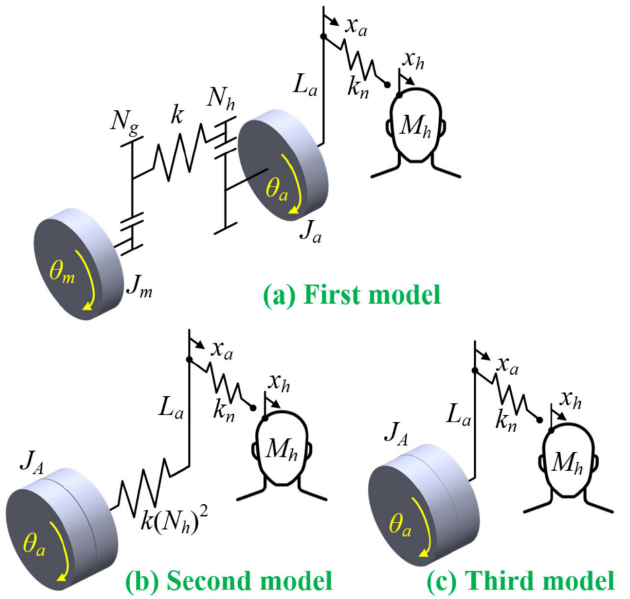

FIGURE 13. Dynamic impact models (a) Compliant actuator (b) SEA (c) Stiff actuator.

Table 6 lists the detailed specifications of the planar springs and elastic elements. For the large compliant actuator, the outer diameter of the elastic element (65 mm) is much smaller than that of the elastic element (10.16 mm) in [17]. For the small compliant actuator, the outer diameter of the elastic element is 28 mm with a thickness of merely 6 mm. The maximum allowable elastic element deformation for both actuators is ±20°. Each planar spring contributes ±10°.

Each planar spring in Fig. 11(a) includes two deformable limbs connecting the outer and inner rings. The shape and arrangement of the deformable limbs are based on the topology developed in [33], where the linearity of the torque to the deformation curve is ensured by placing the deformable limbs symmetrically. Unlike the planar spring in [16] that employs symmetric limbs, the proposed planar spring uses asymmetric limbs to allow the elastic element to have larger deformation when compared with that in [16]. To minimize the bearing loading of the first and second geartrains, the two planar springs in Fig. 11(a) are oriented such that the unwanted radial forces of the two planar springs cancel. Heat-treated plastic mold steel (S-STAR-A) is used as the material for the planar springs. The planar spring is fabricated using wire electrical discharge machining.

TABLE 7. Comparison of impact parameters of different robot actuators (Unit of HIC_{36}: s).

Actuator type	Inertia (kgm^2)	Eq.	Fig.	HIC_{36}
I. Our large compliant actuator (k = 14.97 Nm/rad)	$J_a = 1.0$; $J_m = 9.9 \times 10^{-5}$	(9)	13(a)	6.88
II. SEA ($k(N_h)^2$ = 38937 Nm/rad)	$J_A = 2.03$	(11)	13(b)	6.47
III. Our large stiff actuator ($k = \infty$)	$J_A = 2.03$	(12)	13(c)	15.70
IV. KUKA LWR4+ (J_1)	$J_A = 3.19$	(12)	13(c)	27.43
V. UR10 (J_1)	$J_A = 10.05$	(12)	13(c)	82.96

Figs. 11(b) and 11(c) show the deformed shapes of the planar springs when the inner ring is fixed, and a 10° rotation is given to the outer ring in the counterclockwise direction. The total stiffnesses of the elastic elements are 14.97 Nm/rad and 1.13 Nm/rad, respectively. When the maximum deformation of the planar spring is reached, the maximum equivalent stress is 1036.8 MPa for the large compliant actuator and 1109.8 MPa for the small actuator. These maximum equivalent stresses have been designed to be smaller than the yield stress of the material (1540 MPa). Fig. 12 further shows the experimental torque-to-deformation curves of the elastic elements of both compliant actuators. Both curves show good linearity due to the symmetric arrangement of the deformable limbs.

IV. EFFECTS OF INERTIA AND COMPLIANCE ON THE HUMAN-ROBOT IMPACT

A. DYNAMIC IMPACT MODELS AND NUMERICAL COMPARISONS

Various metrics [34] have been developed to evaluate the unexpected collision between humans and robots. To study the effects of low inertia and compliance of the proposed actuators on human-robot collision safety, we implement the head injury criterion (HIC) [35], [36], which can be expressed as follows.

$$\mathrm{HIC}_{\Delta t_{\max}} = \max_{t_1,t_2}\left[\left(\frac{1}{t_2-t_1}\int_{t_1}^{t_2}\ddot{x}_h dt\right)^{2.5}(t_2-t_1)\right]$$
$$\text{subject to } t_2 - t_1 = \Delta t \le \Delta t_{\max} \tag{7}$$

where t is the accumulated time over the impact duration, $\ddot{x}_h$ is the human head acceleration in terms of gravitational acceleration ($g = 9.8$ m/s^2). Symbols t_1 and t_2 are two time instants selected to maximize the value of HIC. In this paper, we select $\Delta t_{\max}$ as 36 ms such that the head injury criterion is denoted as HIC_{36}. The HIC_{36} value should be as small as possible to reduce any harm to a human operator. A value of HIC_{36} above 100 is considered unsuitable for normal operation.

Fig. 13 shows three dynamic models for the impact analysis between the compliant actuator and the human operator. For all three models, the human head is treated as a point mass with $M_h = 4$ kg. The actuator impacts the human head through a rigid and massless link with a length of L_a. The environmental stiffness k_n accounts for the equivalent impact stiffness due to the stiffness k_f of the flex spline of the harmonic drive.

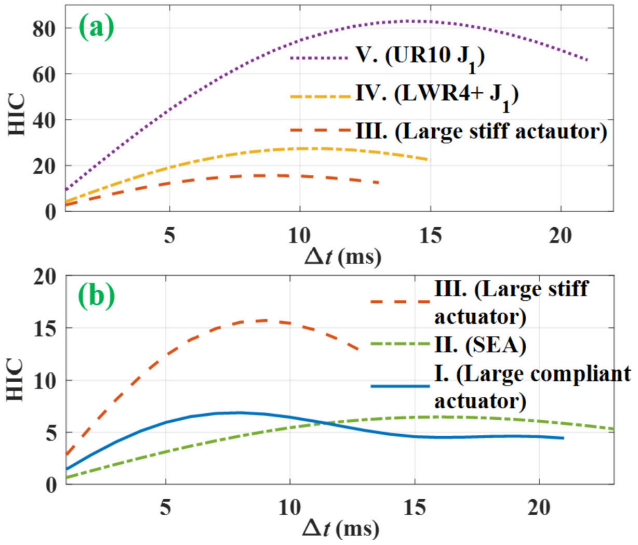

FIGURE 14. Comparison of HIC values (a) Effect of actuator inertia (b) Effect of actuator compliance.

$$k_n = k_f / L_a^2 \tag{8}$$

For a link length of $L_a = 1.3$ m and flex spline stiffness of 8.8×10^4 Nm/rad according to Table 1, the stiffness k_n would be 52071 N/m.

We ignore the effects of geartrain efficiency and viscous friction for the first impact model in Fig. 13(a). The equations governing the impact dynamics of the compliant actuator can be rewritten from Eqs. (1)-(2) as follows.

$$\begin{aligned}\ddot{\theta}_m &= -(\theta_m/N_g - N_h\theta_a)k/J_m N_g \\ \ddot{\theta}_a &= -(N_h\theta_a - \theta_m/N_g)kN_h/J_a + F_a L_a/J_a \\ \ddot{x}_h &= -F_a/M_h\end{aligned} \tag{9}$$

where F_a denotes the impact force from the human head to the actuator. The impact force F_a can be expressed as follows.

$$x_a = L_a\theta_a;\ F_a = \begin{cases} k_n(x_h - x_a) & \text{when } x_a \ge x_h \\ 0 & \text{when } x_a < x_h \end{cases} \tag{10}$$

where x_h is the displacement of the head. For the second impact model in Fig. 13(b), the elastic element is placed on the output side of the compliant actuator. The stiffness of the elastic element is $k(N_h)^2$ in order to match the model in Fig. 13(a). The second model is to emulate existing SEAs, as shown in Fig. 10(a). The dynamic equations for the second model are as follows.

$$\ddot{\theta}_a = [F_a L_a + kN_h^2(x_a/L_a - \theta_a)]/J_A;\ \ddot{x}_h = -F_a/M_h \tag{11}$$

where J_A is the total reflected inertia of the actuator. For the third impact model in Fig. 13(c), we consider a stiff actuator where the only compliance comes from k_n. The dynamic equations for the third model are as follows.

$$\ddot{\theta}_a = F_a L_a/J_A;\ \ddot{x}_h = -F_a/M_h \tag{12}$$

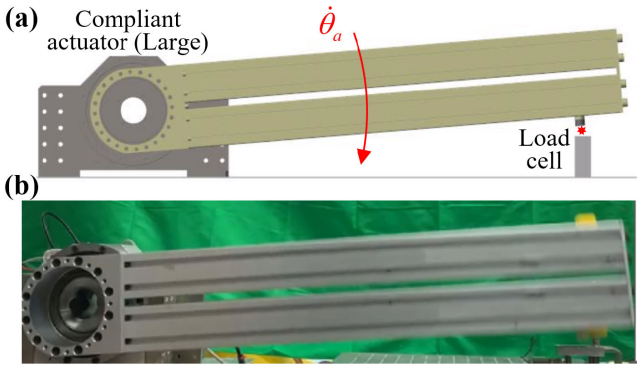

FIGURE 15. (a) Setup of actuator impact experiment (b) Snapshot of impact experiment.

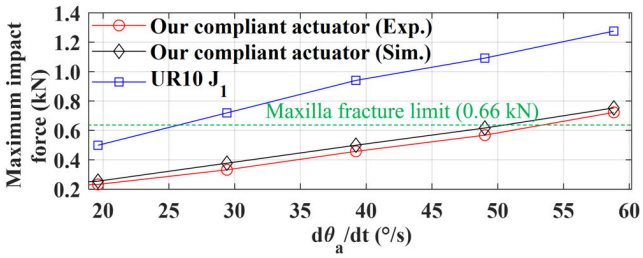

FIGURE 16. Comparison of simulation and experimental impact forces.

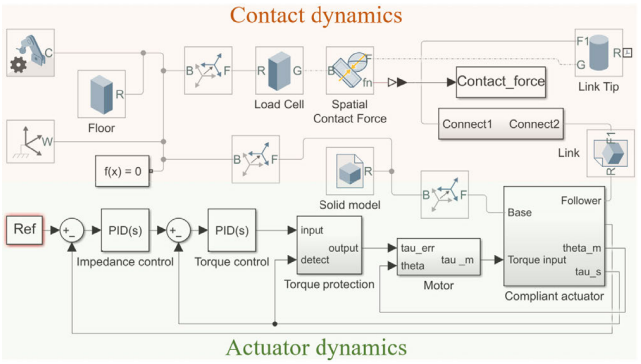

FIGURE 17. Simscape model of actuator impact.

For all three models, we consider the case where the output link is controlled at an initial velocity of $d\theta_a(0)/dt = 17$ rpm. The human head is initially at a speed of -2 m/s to emulate a normal human walking speed. Other initial conditions required to solve Eqs. (9), (11), and (12) are given as follows.

$$\theta_m(0) = \theta_a(0) = x_h(0) = 0; \dot{\theta}_m(0) = N_g N_h \dot{\theta}_a(0) \qquad (13)$$

We compare five different human-actuator impact results based on the three models in Fig. 13. Table 7 lists the actuator parameters. Actuator I is our larger compliant actuator. The inertia values of Actuators II and III are the same as Actuator I, except that the stiffness of the elastic element is 38937 Nm/rad for Actuator II and infinity for Actuator III. Actuators I, II, and III correspond to the models in Figs. 13(a), 13(b), and 13(c), respectively. Actuators I and II have the same effective stiffnesses. Actuators IV and V are the J_1 joint from the KUKA LWR4+ robot and UR10 robot, respectively. The values of J_A are from Table 3. Actuators IV and V are stiff actuators using the model in Fig. 13(c).

To evaluate the effect of actuator inertia, Fig. 14(a) compares the HIC curves of Actuators III, IV, and V. Each curve terminates when the head and actuator are separated. The values of HIC_{36} are given in Table 7. As expected, our large actuator has a much lower inertia, and thus the HIC_{36} value is significantly lower than those of Actuators IV and V. Hence, our large actuator can achieve safer human-robot interaction even without the elastic element.

Fig. 14(b) compares the HIC curves of Actuators I, II, and III to evaluate the effect of actuator compliance. Regardless of the location of the elastic element, Actuators I and II both achieve much lower HIC_{36} values than Actuator III. Hence, the elastic element can effectively provide impact filtering. Since Actuators I and II have similar HIC_{36} values, both models in Fig. 10 can achieve nearly the same impact filtering capability if their effective stiffnesses are the same. The use of the proposed compliant actuator is beneficial because the size of the elastic element can be made smaller. Comparing Actuators I and V, the proposed compliant actuator with low inertia can reduce the HIC_{36} value by more than 90%.

B. ACTUATOR IMPACT EXPERIMENT

An experiment was conducted to verify the results in Sec. IV-A. Fig. 15(a) shows the setup. To emulate the dynamic model in Fig. 13(a), the proposed large compliant actuator was connected to a link with a length of 0.7 m. The actuator rotated the link with a constant angular velocity to impact a load cell (FUTEK LSB200). Fig. 15(b) shows a snapshot of the impact experiment. The maximum impact force at different angular velocities was recorded using the load cell. Fig. 16 shows the experimental results. As expected, the impact force increases with the increase of angular velocities. Simulation results are also plotted in Fig. 16. Using the same parameters as the experiment, the simulation results are obtained using MATLAB Simscape. Fig. 17 shows the Simscape model. The upper half in Fig. 17 is used to model the contact dynamics, whereas the bottom half in Fig. 17 is used to model the actuator dynamics. The parameters of the large compliant actuator are from Table 1. For the contact dynamics, the contact stiffness between the link and load cell was set at 10^6 N/m to emulate the stiffness of the link's tip. Both experimental and simulation results agree well, which verifies the dynamic impact model in Fig. 13.

Fig. 16 further compares the impact force of our large compliant actuator with that of the J_1 joint from the UR10 robot. The simulation parameters of the UR10 robot are from Table 3. At various speeds, the maximum impact force of our large compliant actuator is nearly half of that of the J_1 joint from the UR10 robot. To evaluate the effect of impact force on human injury, the maxilla is used as an example because it is the weakest bone of the human head. The maxilla fracture limit of 0.66 kN [36] is shown in Fig. 16. The impact force of the proposed compliant actuator is below the limit

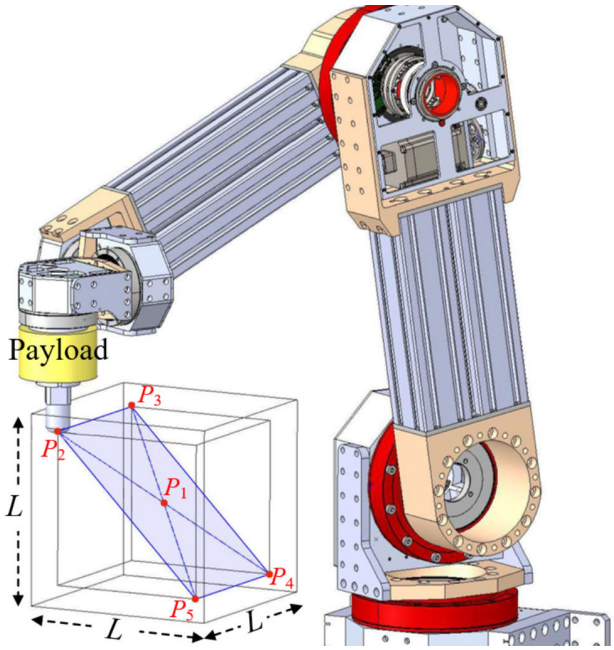

FIGURE 18. Experimental setup of pose repeatability.

at almost all speeds. By contrast, the impact force of the J_1 joint from the UR10 robot is above the fracture limit at almost all speeds. Hence, the proposed compliant actuator can effectively prevent human injury when compared with stiff actuators.

V. EXPERIMENTAL VERIFICATION OF POSE REPEATABILITY

This section aims to show that the robot can maintain a high level of pose repeatability at the end-effector although the actuators are inherently compliant with low inertia. Fig. 18 shows the experimental setup of pose repeatability. A payload of 2 kg was mounted on the robot end-effector. The tip of the end-effector was programmed to move successively from pose P_1 to pose P_5. The five poses form a diagonal plane inside a cube with a side length of L. Pose P_1 is the center of the diagonal plane and the other four poses are at the four corners. The distance between P_2 and P_3 is $0.8L$, whereas the distance between P_3 and P_4 is $1.13L$. The average travel speed was 60 mm/s from one pose to another. A total of 30 cycles were carried out. As shown in Fig. 19, the position of the end-effector was obtained using a FARO Vantage laser tracker.

Fig. 20 shows the controller diagram for the pose repeatability experiment. Given a required end-effector trajectory $\boldsymbol{P_r}$, the controller can be used to generate a specified end-effector stiffness $\boldsymbol{K_w}$ during the end-effector motion.

$$\boldsymbol{K_w} = \boldsymbol{diag}(K_x, K_y, K_z, K_\alpha, K_\beta, K_\gamma) \tag{14}$$

Variables K_x, K_y, and K_z are the linear stiffnesses of the end-effector, whereas variables K_α, K_β, and K_γ are the rotational stiffnesses of the end-effector. The Jacobian matrix $\boldsymbol{J}$ is calculated using the D-H parameters in Table 4. Variables $\boldsymbol{\theta_a}$,

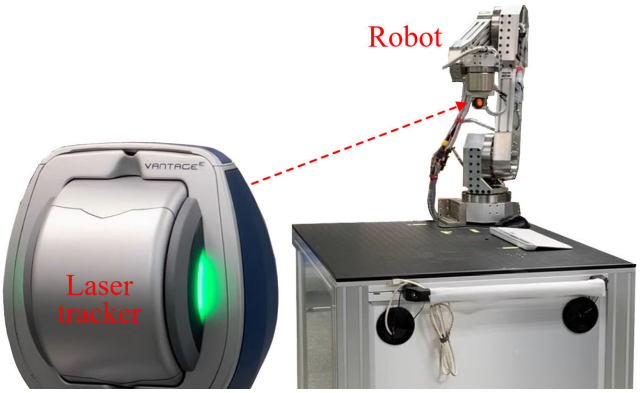

FIGURE 19. Laser tracker and the compliant robot.

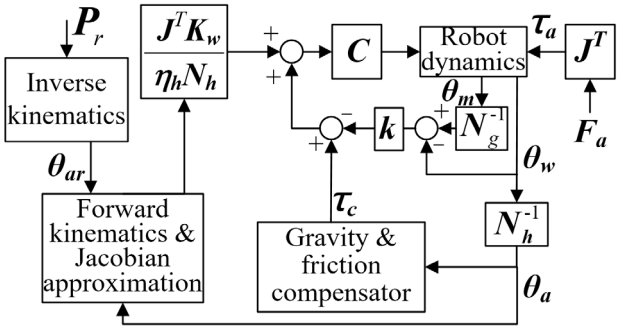

FIGURE 20. Controller diagram of the compliant robot.

$\boldsymbol{\theta_m}$, $\boldsymbol{\theta_w}$, $\boldsymbol{\eta_h}$, $\boldsymbol{N_h}$, $\boldsymbol{N_g}$, $\boldsymbol{k}$, and τ_a are the vector forms of the parameters defined in Eqs. (1)-(2). The inner feedback loop includes a torque controller $\boldsymbol{C}$ and compensation torque τ_c to ensure the accuracy of stiffness control. For simplicity of control, only proportional gains are used for $\boldsymbol{C}$. The values of the proportional gains are 5 and 2 for the large and small compliant actuators, respectively. The robot dynamics is modeled using Eqs. (1)-(2) for each actuator. The stiffness $\boldsymbol{K_w}$ should be set high to ensure good position control performance and set low to ensure safer human-robot interaction [37]. For the repeatability experiment, the end-effector stiffness values were 10^5 N/m in the linear directions and 1.5×10^3 Nm/rad in the rotational directions. These stiffness values were experimentally chosen to ensure high stiffness of the robot end-effector without causing instability within its range of motion.

According to the ISO 9283:1998 standard [38], the pose repeatability (RP) can be defined as follows.

$$RP = \bar{\ell} + 3S_\ell \tag{15}$$

where $\bar{\ell}$ is the mean value and S_ℓ is the standard deviation that can be expressed as follows.

$$\begin{aligned} &S_\ell = \sqrt{\left[\sum_{j=1}^{n} \left(\ell_j - \bar{\ell}\right)^2\right]/(n-1)}; \\ &\ell_j = \sqrt{\left[\left(x_j - \bar{x}\right)^2 + \left(y_j - \bar{y}\right)^2 + \left(z_j - \bar{z}\right)^2\right]}; \bar{\ell} = \frac{1}{n}\sum_{j=1}^{n} \ell_j \\ &\bar{x} = \frac{1}{n}\sum_{j=1}^{n} x_j; \bar{y} = \frac{1}{n}\sum_{j=1}^{n} y_j; \bar{z} = \frac{1}{n}\sum_{j=1}^{n} z_j \end{aligned} \tag{16}$$

TABLE 8. Pose repeatability results of the proposed compliant robot (Unit: mm).

Case	P_1	P_2	P_3	P_4	P_5	Avg.
$L = 150$ mm	0.0254	0.0266	0.0292	0.0236	0.0219	0.0253
$L = 200$ mm	0.0408	0.0312	0.0426	0.0413	0.0281	0.0368

TABLE 9. Comparison of pose repeatability of various robots (Unit: mm).

	[7]	[9]	[39]	Our robot	[40]
Actuator type	Compliant			Stiff	
Pose repeatability	0.425	3.7	2.9	0.0368	0.053

Table 8 lists the experimental results of pose repeatability calculated using Eqs. (15)-(16). For the cases of $L = 150$ mm and $L = 200$ mm, the average values of pose repeatability are 0.0253 and 0.0368 mm, respectively. As a comparison, Table 9 lists the pose repeatability of various robots. The Baxter robot [39] applies the existing SEA model in Fig. 10(a). The Baxter robot has a large pose repeatability value of 2.9 mm. The anthropomorphic robot in [7] has low inertia and high stiffness and has a pose repeatability value of 0.425 mm. The compliant robot in [9] also has low inertia but the pose repeatability is 3.7 mm. Although these robots [7], [9], [39] can provide safe human-robot interaction, their repeatability values make them unsuitable for tasks that require precise positioning. By contrast, existing collaborative robots with stiff actuators have a pose repeatability value of 0.053 mm (e.g., Universal robot [40]). Due to the use of the new SEA model in Fig. 10(b), our robot has a superior pose repeatability performance than other types of compliant robots. The repeatability of our robot is also comparable to those of commercially available collaborative robots.

Summarizing the results in Secs. IV and V, the proposed compliant actuators have comparable impact filtering capabilities as existing compliant actuators but much better repeatability performance than existing compliant actuators.

VI. CONCLUSION

This paper has presented a new type of inherently compliant actuator for safer human-robot interaction. To ensure high output torque and high output stiffness, the geartrains and elastic elements have been specifically designed such that both large and small compliant actuators have high torque-to-inertia ratios and low torque-to-stiffness ratios. The torque-to-inertia ratios of the proposed actuators are at least two times that of existing robot actuators. The torque-to-stiffness ratios of the proposed actuators are less than 10% of those of existing SEAs. A robot built using the compliant actuators has a much smaller effective mass sensed at the end-effector. Human-robot impact simulations have shown the effectiveness of the proposed compliant actuators. An experiment has been conducted to verify that the repeatability of the robot is less than 0.0368 mm, which meets the requirement of task precision. It is expected that these new compliant actuators can be applied to build robots for safer human-robot interaction.

REFERENCES

[1] A. T. Vo and H.-J. Kang, "Neural integral non-singular fast terminal synchronous sliding mode control for uncertain 3-DOF parallel robotic manipulators," *IEEE Access*, vol. 8, pp. 65383–65394, 2020.
[2] B. Rouzbeh, G. M. Bone, G. Ashby, and E. Li, "Design, implementation and control of an improved hybrid pneumatic-electric actuator for robot arms," *IEEE Access*, vol. 7, pp. 14699–14713, 2019.
[3] D. Rodriguez-Guerra, G. Sorrosal, I. Cabanes, and C. Calleja, "Human–robot interaction review: Challenges and solutions for modern industrial environments," *IEEE Access*, vol. 9, pp. 108557–108578, 2021.
[4] K. Qi, Z. Song, and J. S. Dai, "Safe physical human–robot interaction: A quasi whole-body sensing method based on novel laser-ranging sensor ring pairs," *Robot. Comput.-Integr. Manuf.*, vol. 75, Jun. 2022, Art. no. 102280.
[5] J. Li, Y. Guan, H. Chen, B. Wang, T. Zhang, X. Liu, J. Hong, D. Wang, and H. Zhang, "A high-bandwidth end-effector with active force control for robotic polishing," *IEEE Access*, vol. 8, pp. 169122–169135, 2020.
[6] S. Rader, L. Kaul, P. Weiner, and T. Asfour, "Highly integrated sensor-actuator-controller units for modular robot design," in *Proc. IEEE Int. Conf. Adv. Intell. Mechatronics*, 2017, pp. 1160–1166.
[7] Y.-J. Kim, "Anthropomorphic low-inertia high-stiffness manipulator for high-speed safe interaction," *IEEE Trans. Robot.*, vol. 33, no. 6, pp. 1358–1374, Dec. 2017.
[8] G. Zhang, Q. Tong, T. Zhang, J. Tao, and A. Qiu, "Design of a high torque density robot joint and analysis of force control method applied for a light exoskeleton," *Electronics*, vol. 12, no. 2, p. 397, Jan. 2023.
[9] D. V. Gealy, S. McKinley, B. Yi, P. Wu, P. R. Downey, G. Balke, A. Zhao, M. Guo, R. Thomasson, A. Sinclair, P. Cuellar, Z. McCarthy, and P. Abbeel, "Quasi-direct drive for low-cost compliant robotic manipulation," in *Proc. Int. Conf. Robot. Autom. (ICRA)*, May 2019, pp. 437–443.
[10] C.-T. Chen, W.-Y. Lien, C.-T. Chen, M.-J. Twu, and Y.-C. Wu, "Dynamic modeling and motion control of a cable-driven robotic exoskeleton with pneumatic artificial muscle actuators," *IEEE Access*, vol. 8, pp. 149796–149807, 2020.
[11] G. A. Pratt and M. M. Williamson, "Series elastic actuators," in *Proc. IEEE/RSJ Int. Conf. Intell. Robots Syst. Human Robot Interact. Cooperat. Robots*, vol. 1, Aug. 1995, pp. 399–406.
[12] S. Li, J. Li, G. Tian, and H. Shang, "Stiffness adjustment for a single-link robot arm driven by series elastic actuator in muscle training," *IEEE Access*, vol. 7, pp. 65029–65039, 2019.
[13] Y.-H. Lai, S.-Y. Huang, and C.-C. Lan, "A force-controlled parallel robot for large-range stiffness rendering in three dimensions," *IEEE Robot. Autom. Lett.*, vol. 7, no. 2, pp. 1340–1347, Apr. 2022.
[14] J. D. G. Fernández, B. Yu, V. Bargsten, M. Zipper, and H. Sprengel, "Design, modelling and control of novel series-elastic actuators for industrial robots," *Actuators*, vol. 9, no. 1, p. 6, Jan. 2020.
[15] N. G. Tsagarakis, D. G. Caldwell, F. Negrello, W. Choi, L. Baccelliere, V. G. Loc, J. Noorden, L. Muratore, A. Margan, A. Cardellino, and L. Natale, "Walk-man: A high-performance humanoid platform for realistic environments," *J. Field Robot.*, vol. 34, no. 7, pp. 1225–1259, Oct. 2017.
[16] N. Kashiri, J. Malzahn, and N. G. Tsagarakis, "On the sensor design of torque controlled actuators: A comparison study of strain gauge and encoder-based principles," *IEEE Robot. Autom. Lett.*, vol. 2, no. 2, pp. 1186–1194, Apr. 2017.
[17] N. Paine, J. S. Mehling, J. Holley, N. A. Radford, G. Johnson, C. Fok, and L. Sentis, "Actuator control for the NASA-JSC valkyrie humanoid robot: A decoupled dynamics approach for torque control of series elastic robots," *J. Field Robot.*, vol. 32, no. 3, pp. 378–396, May 2015.
[18] E. Dunwoodie, R. Mutlu, B. Ugurlu, M. Yildirim, T. Uzunovic, and E. Sariyildiz, "A high-torque density compliant actuator design for physical robot environment interaction," in *Proc. IEEE 16th Int. Workshop Adv. Motion Control (AMC)*, Sep. 2020, pp. 1–6.
[19] C.-H. Huang, K.-W. Chiao, C.-P. Yu, Y.-C. Kuo, and C.-C. Lan, "A variable-stiffness robot for force-sensitive applications," *IEEE/ASME Trans. Mechatronics*, vol. 28, no. 4, pp. 1–9, 2023.

[20] Y.-S. Lee, K.-W. Chiao, and C.-C. Lan, "A hybrid impedance controller for series elastic actuators to render a wide range of stable stiffness in uncertain environments," *IEEE Robot. Autom. Lett.*, vol. 6, no. 2, pp. 739–746, Apr. 2021.
[21] B. Vanderborght, A. Albu-Schäffer, A. Bicchi, E. Burdet, D. G. Caldwell, R. Carloni, M. Catalano, O. Eiberger, W. Friedl, G. Ganesh, and M. Garabini, "Variable impedance actuators: A review," *Robot. Auto. Syst.*, vol. 61, no. 12, pp. 1601–1614, 2013.
[22] N. Govindan, S. Ramesh, and A. Thondiyath, "Design of a variable stiffness joint module to quickly change the stiffness and to reduce the power consumption," *IEEE Access*, vol. 8, pp. 138318–138330, 2020.
[23] I. Hussain, A. Albalasie, M. I. Awad, K. Tamizi, Z. Niu, L. Seneviratne, and D. Gan, "Design and control of a discrete variable stiffness actuator with instant stiffness switch for safe human–robot interaction," *IEEE Access*, vol. 9, pp. 118215–118231, 2021.
[24] J. Guo and J. Guo, "Mechanical structure design and actuation characteristics analysis of the parallel driven variable stiffness actuator with unrestricted rotation range of the output shaft," *IEEE Access*, vol. 10, pp. 83529–83566, 2022.
[25] A. Scibilia, M. Valori, N. Pedrocchi, I. Fassi, S. Herbster, R. Behrens, J. Saenz, A. Magisson, C. Bidard, M. Kuhnrich, A. B. Lassen, and K. Nielsen, "Analysis of interlaboratory safety related tests in power and force limited collaborative robots," *IEEE Access*, vol. 9, pp. 80873–80882, 2021.
[26] C.-C. Chung, C.-H. Huang, and C.-C. Lan, "A torque-controlled actuator with high rigidity and low aspect ratio," *IEEE/ASME Trans. Mechatronics*, vol. 27, no. 6, pp. 5572–5582, Dec. 2022.
[27] K.-Y. Lin, C.-C. Chung, and C.-C. Lan, "Improving the dynamic force control of series elastic actuation using motors of high torque-to-inertia ratios," *IEEE Access*, vol. 8, pp. 6968–6977, 2020.
[28] J. Li, D. Cong, Y. Yang, and Z. Yang, "A hydraulic actuator for joint robots with higher torque to weight ratio," *Robotica*, vol. 41, no. 2, pp. 756–774, pp. 1–19.
[29] M. Ganglbauer, M. Ikeda, M. Plasch, and A. Pichler, "Human in the loop online estimation of robotic speed limits for safe human robot collaboration," *Proc. Manuf.*, vol. 51, pp. 88–94, Jan. 2020.
[30] T. P. Jitendra, A. A. Selvakumar, and J. A. C. Ramon, "Manipulation and path planning for KUKA (LWR/LBR 4+) robot in a simulated and real environment," *J. Autom., Mobile Robot. Intell. Syst.*, vol. 11, no. 3, pp. 15–21, Nov. 2017.
[31] S. Rader, L. Kaul, H. Fischbach, N. Vahrenkamp, and T. Asfour, "Design of a high-performance humanoid dual arm system with inner shoulder joints," in *Proc. IEEE-RAS 16th Int. Conf. Humanoid Robots (Humanoids)*, Nov. 2016, pp. 523–529.
[32] A. Jubien, M. Gautier, and A. Janot, "Dynamic identification of the kuka LWR robot using motor torques and joint torque sensors data," *IFAC Proc. Volumes*, vol. 47, no. 3, pp. 8391–8396, 2014.
[33] Y.-L. Yu and C.-C. Lan, "Design of a miniature series elastic actuator for bilateral teleoperations requiring accurate torque sensing and control," *IEEE Robot. Autom. Lett.*, vol. 4, no. 2, pp. 500–507, Apr. 2019.
[34] J. Versace, "A review of the severity index," in *Proc. 15th Stapp CarCrash Conf.*, New York, NY, USA, 1971.
[35] A. Bicchi and G. Tonietti, "Fast and 'soft-arm' tactics [robot arm design]," *IEEE Robot. Autom. Mag.*, vol. 11, no. 2, pp. 22–33, Jun. 2004.
[36] S. Haddadin, A. Albu-Schaffer, and G. Hirzinger, "The role of the robot mass and velocity in physical human–robot interaction—Part I: Non-constrained blunt impacts," in *Proc. IEEE Int. Conf. Robot. Autom.*, May 2008, pp. 1331–1338.
[37] C. Della Santina, M. Bianchi, G. Grioli, F. Angelini, M. Catalano, M. Garabini, and A. Bicchi, "Controlling soft robots: Balancing feedback and feedforward elements," *IEEE Robot. Autom. Mag.*, vol. 24, no. 3, pp. 75–83, Sep. 2017.
[38] *Manipulating Industrial Robots-Performance Criteria and Related Test Methods*, International Organization of Standards, Standards ISO 9283, 1998.
[39] K. S. Chen, "Application of the ISO 9283 standard to test repeatability of the Baxter robot," Thesis, Univ. Illinois Urbana-Champaign, Urbana, IL, USA, 2015.
[40] M. Pollák, M. Košičko, D. Pauličin, and P. Baron, "Measurement of unidirectional pose accuracy and repeatability of the collaborative robot UR5," *Adv. Mech. Eng.*, vol. 12, no. 12, Dec. 2020, Art. no. 168781402097289.

CHEN-PIN YU received the B.S. degree in mechanical engineering from National Cheng Kung University, Taiwan, in 2021, where she is currently pursuing the M.S. degree in mechanical engineering. Her current research interests include robot kinematics, robot dynamics, and actuators.

CHUN-HUNG HUANG received the B.S. degree in mechanical engineering from National Cheng Kung University, Taiwan, in 2021, where he is currently pursuing the M.S. degree in mechanical engineering. His current research interests include mechanism design, robotics, and actuators.

CHAO-CHIEH LAN (Senior Member, IEEE) received the B.S. degree in mechanical engineering from National Taiwan University, Taiwan, in 2000, and the Ph.D. degree in mechanical engineering from the Georgia Institute of Technology, in 2006. He is currently a Professor with the Department of Mechanical Engineering, National Cheng Kung University, Taiwan. His current research interests include compliant actuators, robotic manipulators, and mechanism dynamics.